

Supporting information

Coverage of Capping Ligands Determining Selectivity of Multi-Carbon Products and Morphological Evolution of Cu Nanocatalysts in Electrochemical Reduction of CO₂

Yusik Oh^a, Jiwon Park^a, Yohan Kim^a, Minyoung Shim^a, Taek-Seung Kim^{a,b}, Jeong Young Park^{a,b}, and Hye Ryung Byon^{a*}

^aDepartment of Chemistry, Korea Advanced Institute of Science and Technology (KAIST), 291 Daehak-ro, Yuseong-gu, Daejeon 34141, Republic of Korea

^bCenter for Nanomaterials and Chemical Reactions, Institute for Basic Science (IBS), Daejeon 34141, Republic of Korea.

* E-mail : hrbyon@kaist.ac.kr

The effect of capping ligands through air oxidation of Cu nanoparticles (NPs)

When the Cu NPs were stored in hexane, Cu_2O gradually developed.^{1, 2} After six weeks, the XRD pattern of Cu_2O became pronounced (**Figure S1c**) and the NP surfaces roughened (**Figure S1d**). The UV-vis extinction spectrum signal also shifted to lower energy due to the intensity of the Cu_2O refraction (**Figure S1e**).^{3, 4} The surface oxidation when exposed to air was ascribed to desorption of TDP from the Cu surface.^{1, 2, 5} This resulted in ~16% reduction in the P/Cu atomic ratio compared to the as-prepared material after 4 weeks, and ~29% reduction after 16 weeks (**Figure S1f**). This TDP elimination causes significant CO_2RR selectivity. We prepared almost monolayered Cu NP arrays by depositing $50 \mu\text{g cm}^{-2}$ on porous carbon substrates through a drop-casting method (**Figure S2a**). Upon CO_2RR at -0.98 V against a reversible hydrogen electrode (RHE) using a H-cell (**Figure S3**), the reaction involving as-prepared Cu NPs resulted in FEs of 39.4% CO (FE_{CO}), 43.1% hydrogen gas (FE_{H_2}), and 15.4% formate ($\text{FE}_{\text{HCOO}^-}$), while the C_{2+} product yields were negligible (**Figure S2b**). In contrast, the $\text{FE}_{\text{C}_{2+}}$ of the 1 week- and 6 week-stored Cu NPs were 23.0% and 46.4%, respectively. This demonstrates increasing C_{2+} selectivity with diminishing surface coverage by the capping ligand.

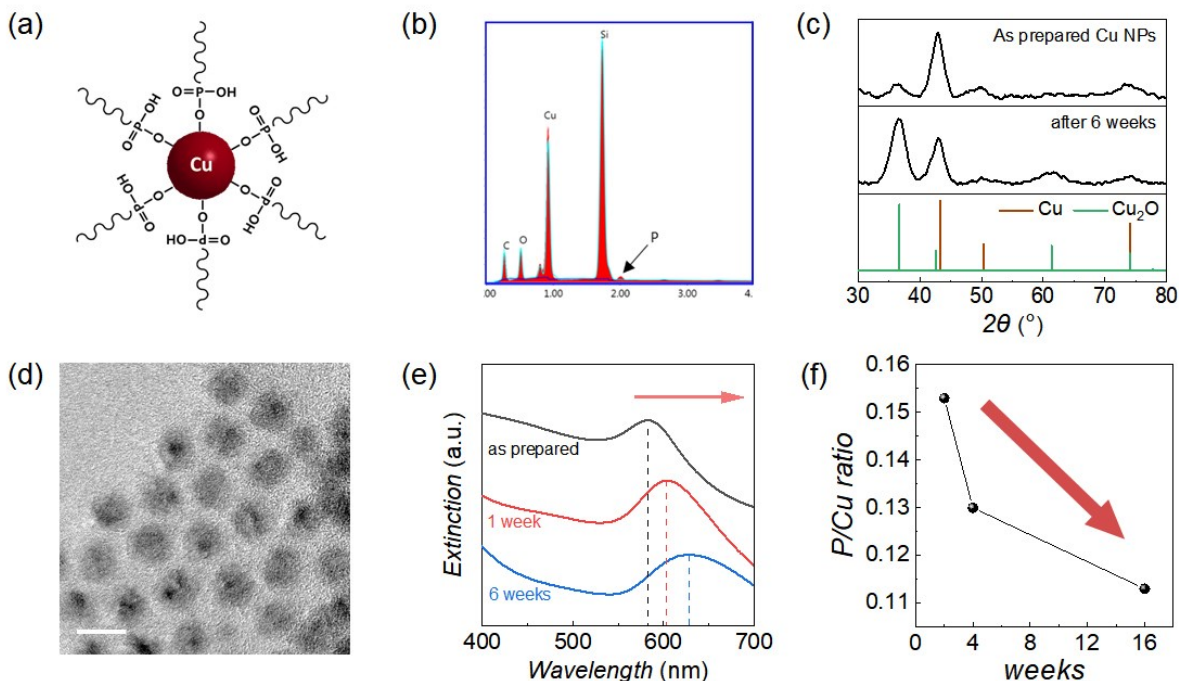


Figure S1. Characterizations of pristine Cu NPs. (a) Schematic illustration of TDP embedded in Cu NP. (b) Energy-dispersive spectroscopy (EDS) of pristine Cu NPs on Si wafer. The Cu (0.95 keV) and O (0.45 keV) arose from Cu₂O, Si (1.80 keV) was from the wafer, and a small phosphorus signal (2.01 keV) is assigned to TDP. (c) XRD patterns of as-prepared Cu NPs (top), stored Cu NPs for 6 weeks in hexane (middle). The Cu NPs dried in a vacuum at r. t. before taking XRD. The metallic Cu reflections of 111, 200, and 220 appear at 43.3°, 50.3°, and 74°, respectively, and the 111 reflection of cuprous oxide (Cu₂O) emerges at 36.6°. The reference patterns of Cu (JCPDS no.85-1326) and Cu₂O (JCPDS no. 77-0199). (d) TEM image of Cu NPs after a 6-week store in hexane. The scale bar indicates 20 nm. (e) UV-vis spectra of as-prepared Cu NPs (black), Cu NPs after 1 week (red), and 6 weeks (blue) stored in hexane. The concentration of NPs solution was adjusted to 0.1 wt%. The UV-vis extinction representing surface plasmon resonance (SPR) became redshift during storage by enhanced surface oxidation. (f) P/Cu ratio of Cu NP samples acquired from XPS measurement. The TDP capping agents were detached out from the Cu NPs with increasing storing time.

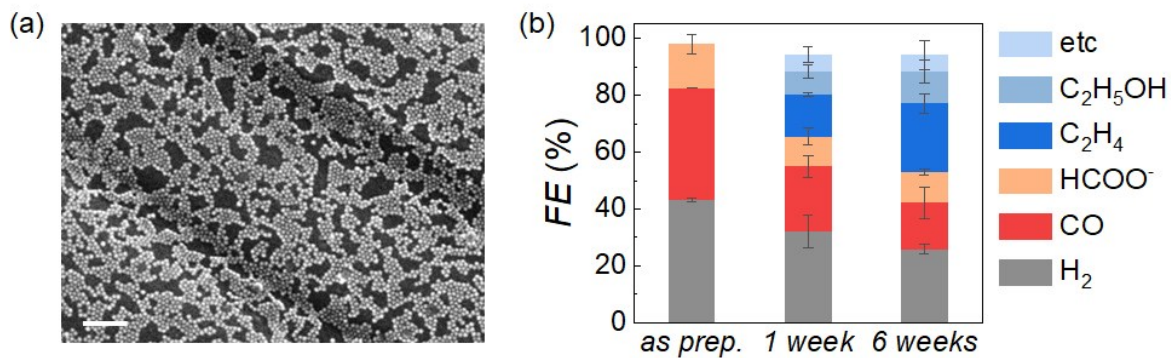


Figure S2. Effect on storing time of Cu NPs for CO₂RR. (a) SEM image of Cu NP electrode. The Cu NPs were stored in hexane for 1 week. The scale bar indicates 100 nm. (b) Comparative CO₂RR products with different aging times in CO₂-saturated 0.1 M KHCO₃(aq) at -0.98 V vs. RHE.

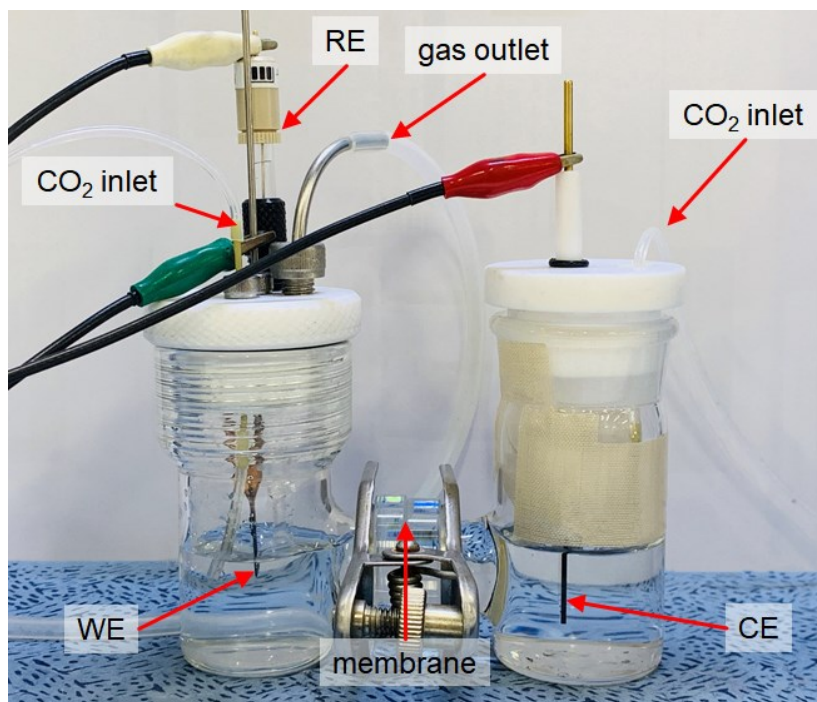


Figure S3. Digital photo of H-cell for CO₂RR examinations.

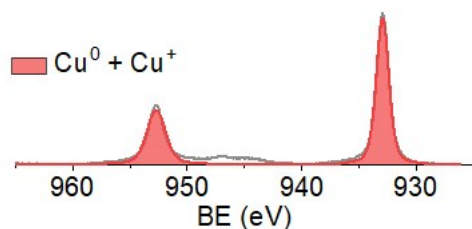


Figure S4. XPS spectrum of Cu 2p BE region for naturally oxidized Cu NPs after 6-weeks storage. The Cu⁰ and Cu⁺ signals are overlapped (~933 eV and ~952.7 eV for 2p_{3/2} and 2p_{1/2}, respectively), while the Cu²⁺ (~935 eV and ~954.3 eV for 2p_{3/2} and 2p_{1/2}, respectively) was marginal.⁶

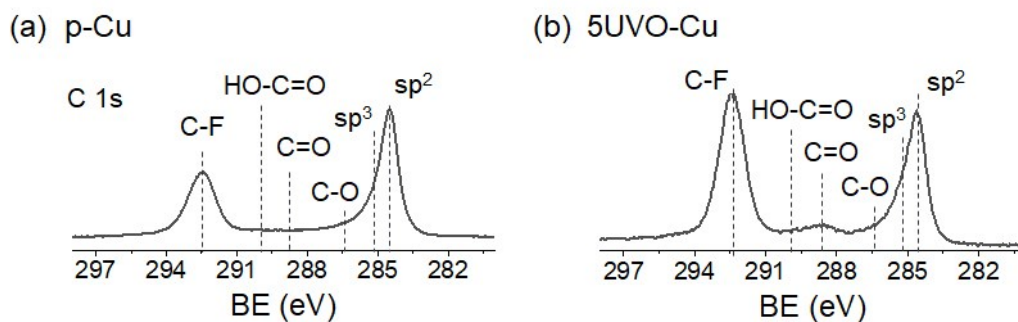


Figure S5. XPS spectra of C 1s binding energy (BE) region for (a) pristine Cu NP electrode (p-Cu) and (b) 5 h UVO-treated Cu NP electrode (5UVO-Cu). The carbon signals including sp², sp³ hybridizations, and C–O arise from GDL.^{7,8} After UVO treatment, the carbonyl group (C=O, ~288.6 eV) newly appeared, in accordance with the C=O in O 1s BE region (**Figure 1c**). Different intensities of C–F implies the non-uniform distribution of PTFE binder on the GDL electrode rather than the UVO influence.⁹ A loss of PTFE from UVO treatment might not be significant.

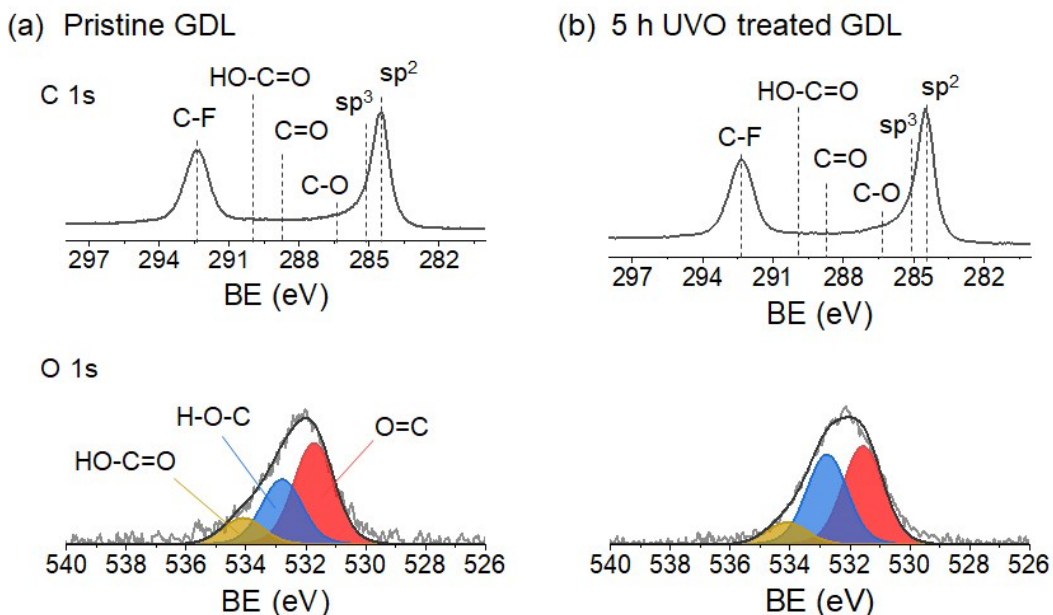


Figure S6. XPS spectra of C 1s and O 1s BE regions for (a) pristine carbon substrate (gas diffusion layer, GDL), including PTFE binder, and (b) the one after 5 h UVO treatment. The C 1s BE spectra of the blank electrodes were assigned to sp^2 -C (~ 284.5 eV), sp^3 -C (~ 285.5 eV), C-O (~ 286.5 eV), C=O (~ 288.6 eV), HO-C=O (~ 290 eV) and C-F (~ 292.4 eV).⁷⁻⁹ The weak C-O and C=O signals were more observed in O 1s BE region, where HO-C=O (~ 534 eV), O-C (~ 533 eV), and O=C (~ 532 eV) peaks were convoluted.¹⁰ After 5 h UVO treatment, an increased C-O signal was detected for both C 1s, and O 1s BE regions. However, the C=O signal was marginally changed.

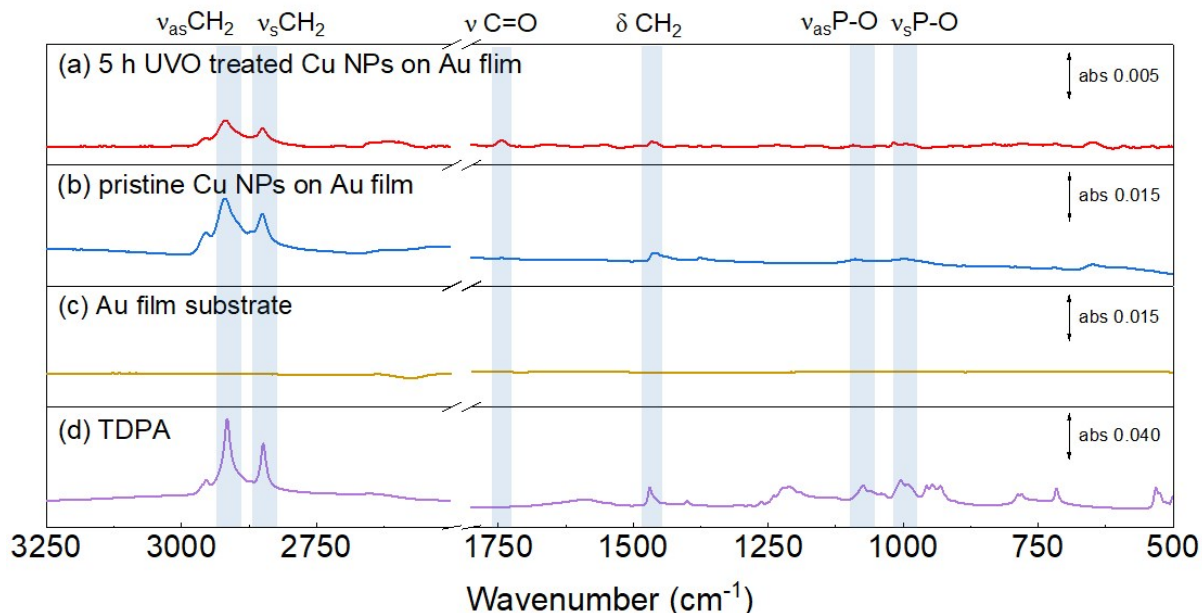


Figure S7. FT-IR spectra of (a) 5 h UVO-treated Cu NPs on gold (Au) film, (b) pristine Cu NPs on Au film (without UVO treatment), (c) pristine Au film, and (d) TDPA powder. The Au film was deposited on Si wafer using electron-beam evaporation, and there was a negligible IR signal of Si. Referring to TDPA precursor, the IR bands of TDP capping agent on Cu NPs were assigned: asymmetric CH_2 stretching mode (ν_{asCH_2} , 2915.7 cm^{-1}), symmetric CH_2 stretching mode (ν_{sCH_2} , 2848.8 cm^{-1}), CH_2 bending mode (δCH_2 , 1469.3 cm^{-1}), asymmetric P–O stretching mode ($\nu_{\text{asP-O}}$, 1073.9 cm^{-1}), and symmetric P–O stretching mode ($\nu_{\text{sP-O}}$, 1004.8 cm^{-1}).¹¹ These signals were attenuated after UVO treatment, while the C=O stretching band ($\nu_{\text{C=O}}$, 1740 cm^{-1}) newly emerged.^{12, 13} It demonstrates the origin of the C=O signal to the decomposition of long hydrocarbon chain of TDP.

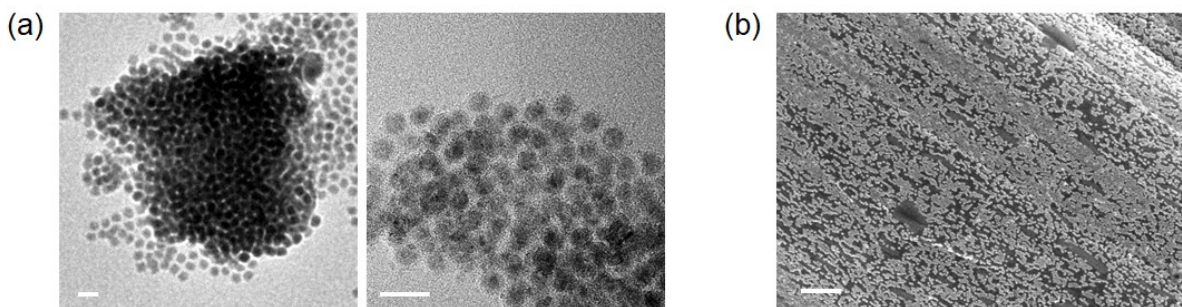


Figure S8. Microscopy images of 5 h UVO-treated Cu NPs. (a) TEM image of 5 h UVO-treated Cu NPs dispersed in hexane. The scale bar indicates 20 nm. (b) SEM image of 5UVO-Cu. The scale bar is 200 nm.

FE (%)	p-Cu	1UVO-Cu	5UVO-Cu	7UVO-Cu
CO	21.23	15.38	12.48	16.37
HCOO ⁻	9.95	8.97	8.30	8.83
CH ₄	1.46	2.14	2.65	2.68
C ₂ H ₄	14.11	24.02	29.33	27.23
C ₂ H ₅ OH	8.74	9.28	11.73	10.73
acetate	0.49	0.71	0.70	0.73
acetone	0.59	0.32	0.41	0.55
ethylene glycol	0.28	0.27	0.22	0.32
allyl alcohol	0.63	0.45	0.85	0.69
n-propanol	4.10	5.82	6.01	5.61
H ₂	33.49	26.87	22.79	21.41
Total	95.07	94.23	95.47	95.15

Table S1. Summary of Faradaic Efficiencies of Cu samples after 3 h CO₂RR at -0.98 V vs. RHE (Figure 2b).

FE (%)	5UVO-Cu, 1.5 h	5UVO-Cu, 3 h
CO	14.09	12.91
HCOO ⁻	8.03	6.92
CH ₄	1.83	1.93
C ₂ H ₄	23.86	30.22
C ₂ H ₅ OH	10.35	12.13
acetate	0.71	0.73
acetone	0.32	0.55
ethylene glycol	N.D.	0.32
n-propanol	5.82	5.61
H ₂	28.78	21.35
Total	93.58	93.88

Table S2. Summary of Faradaic Efficiencies of 5UVO-Cu after 1.5 h and 3 h CO₂RR at -0.98 V vs. RHE. N.D. indicates 'not detected'.

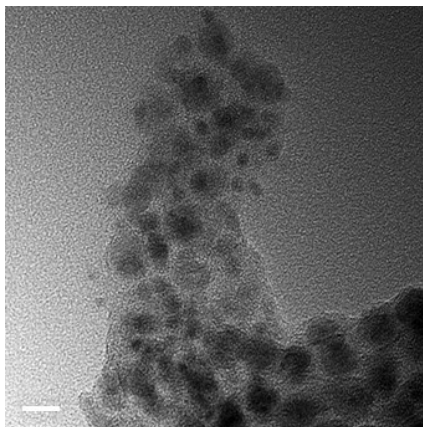


Figure S9. TEM image of 7 h UVO-treated Cu NPs dispersed in hexane, showing coalescence due to long-term irradiation. The scale bar indicates 10 nm.

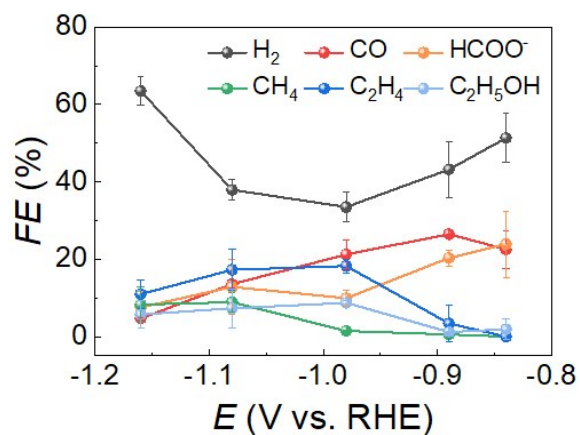


Figure S10. Potential-dependent CO₂RR product distribution for p-Cu. FE_{CO₂RR} was maximum at -0.98 V vs. RHE, with the lowest FE_{H₂}.

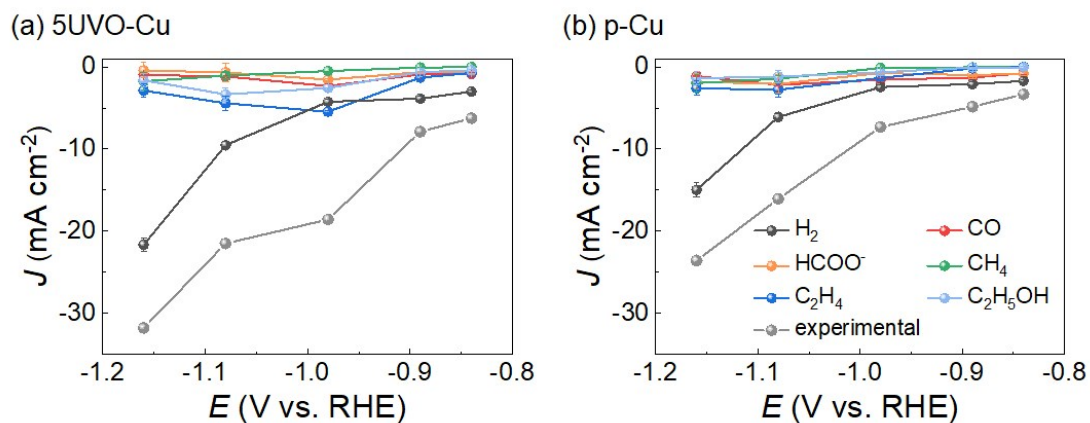


Figure S11. Partial current density (J) of (a) 5 h UVO treated Cu NPs (5UVO-Cu), (b) p-Cu at the different applied potential from -0.84 ~ -1.16 V vs. RHE.

FE (%)	-0.84 V	-0.89 V	-0.98 V	-1.08 V	-1.16 V
CO	13.68	11.38	12.48	5.36	3.02
HCOO ⁻	9.79	7.87	8.30	3.09	1.32
CH ₄	N.D.	0.82	2.65	4.86	5.48
C ₂ H ₄	11.64	16.35	29.33	20.54	9.03
C ₂ H ₅ OH	6.54	7.81	11.73	15.51	5.10
acetate	0.42	0.45	0.70	0.66	0.79
acetone	0.47	0.50	0.41	0.08	0.12
ethylene glycol	0.14	0.20	0.22	0.17	0.17
allyl alcohol	N.D.	N.D.	0.85	N.D.	N.D.
n-propanol	1.80	3.54	6.01	3.93	2.59
H ₂	48.05	48.83	22.79	44.27	68.12
Total	92.53	97.75	95.47	98.47	95.74

Table S3. Summary of Faradaic Efficiencies of 5UVO-Cu at various potentials applied for 3 h CO₂RR (Figure 2c). N.D. indicates ‘not detected’.

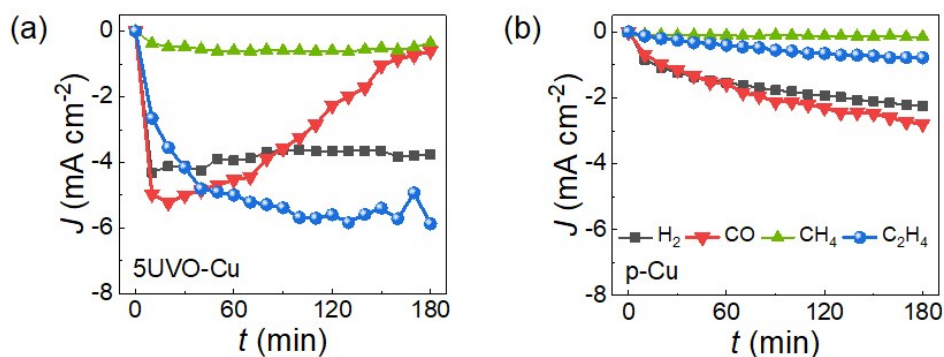


Figure S12. *In situ* variation of partial current density (J) towards gas products during 3 h CO₂RR on (a) 5UVO-Cu and (b) p-Cu at -0.98 V vs. RHE.

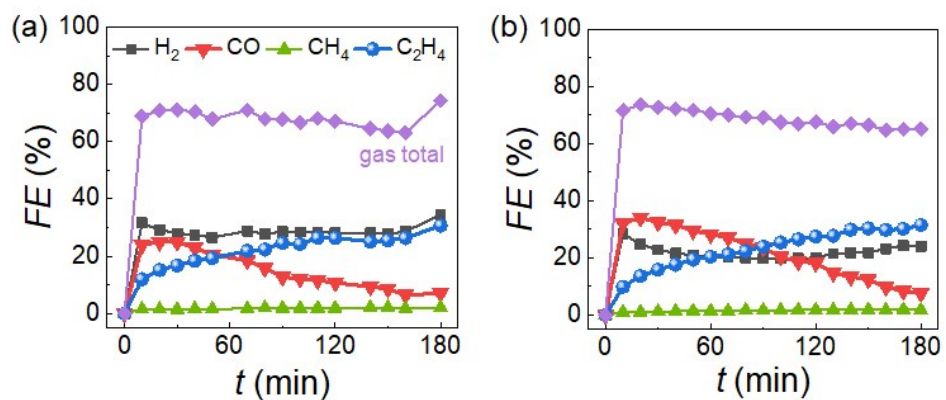


Figure S13. *In situ* analysis of gaseous products from (a) 1UVO-Cu and (b) 7UVO-Cu at -0.98 V vs. RHE. FE_{CO} and $FE_{C_2H_4}$ were inversely crossed after 1 h and 1.5 h CO₂RR for 1UVO-Cu and 7UVO-Cu, respectively.

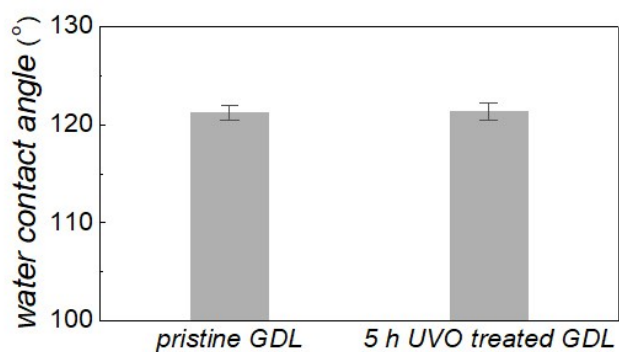


Figure S14. Comparative contact angles of a water droplet on carbon substrate (GDL) before and after UVO treatment. The contact angles were measured 5 times for each substrate. There is a marginal change of hydrophobic surface property before and after 5 h UVO treatment.

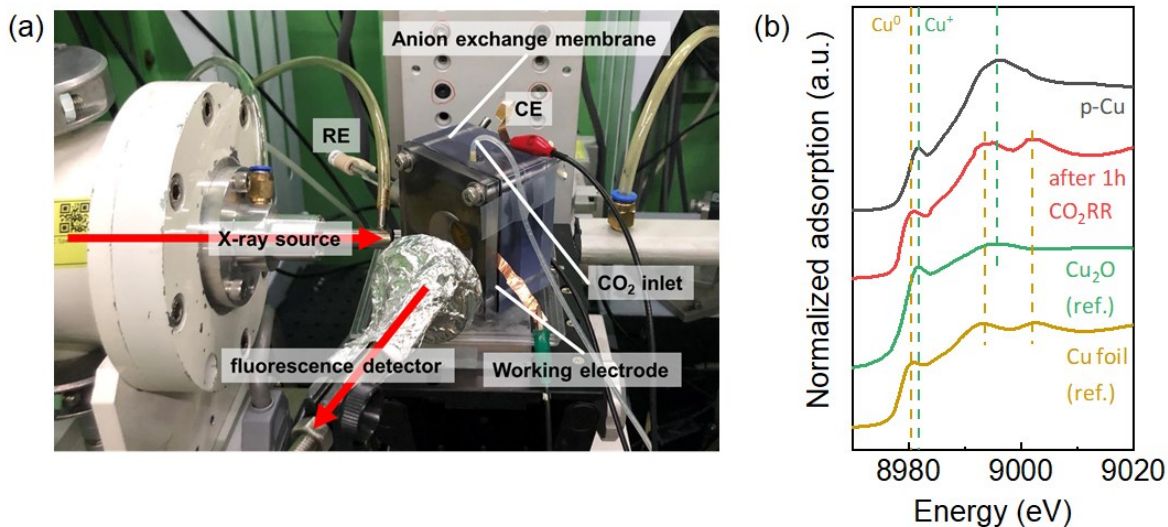


Figure S15. *In situ* X-ray absorption near-edge structure (XANES) analysis of p-Cu. (a) Experimental set-up for *in situ* XANES cell for CO₂RR. The customized two-compartment cell was used. (b) Cu K-edge XANES spectra with the fluorescence mode for p-Cu before CO₂RR and p-Cu electrode after 1 h CO₂RR in the *in situ* XANES cell. These XANES spectra are compared to reference materials, Cu foil, and Cu₂O powder. The p-Cu includes the Cu⁺ species (~8981.8 eV for 1s → 4p_z transition) before CO₂RR. After 1 h CO₂RR, the metallic Cu signal (~8980.6 eV for 1s → 4p_z transition) emerges while the Cu⁺ almost disappears.¹⁴

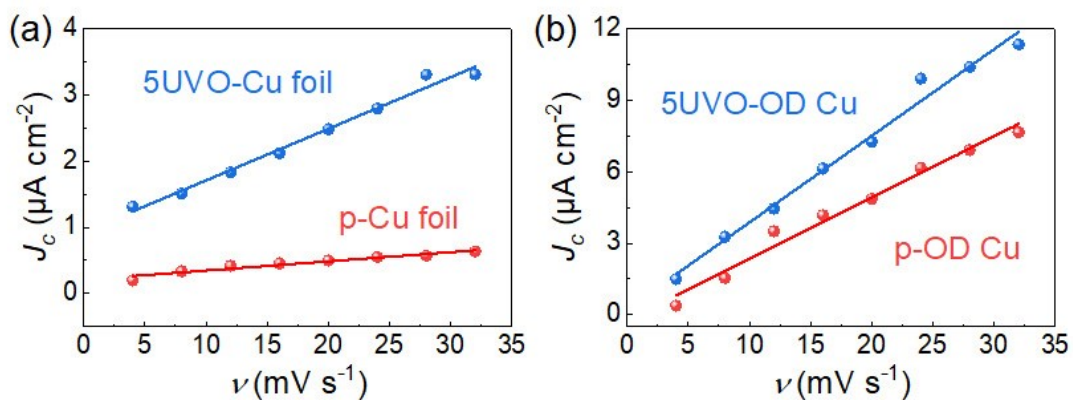


Figure S16. Capacitive current density (J_c) plots for (a) 5 h UVO treated Cu foil (5UVO-Cu foil, blue) and pristine one (p-Cu foil, red) and (b) 5 h UVO treated oxide-derived Cu NPs (5UVO-OD Cu NPs, blue) and pristine one (p-OD Cu NPs, red) as a function of scan rate (ν) at a potential of 0.18 V vs. Ag/AgCl.

	Capacitance ($\mu\text{F cm}^{-2}$)	R^2
p-Cu foil	13.88	0.931
5UVO-Cu foil	77.93	0.983
p-OD Cu NPs	256.84	0.979
5UVO-OD Cu NPs	362.85	0.985

Table S4. The calculated electrochemical capacitance of Cu foil and OD Cu NPs. The slopes of J_c - ν plot in **Figure S16** are electrical double layer capacitance (EDLC), indicating electrochemically active surface area (ECSA) for each sample. The capacitance of Cu foil and OD Cu NPs was ~ 5.6 and ~ 1.4 times increased after 5 h UVO treatment, respectively.

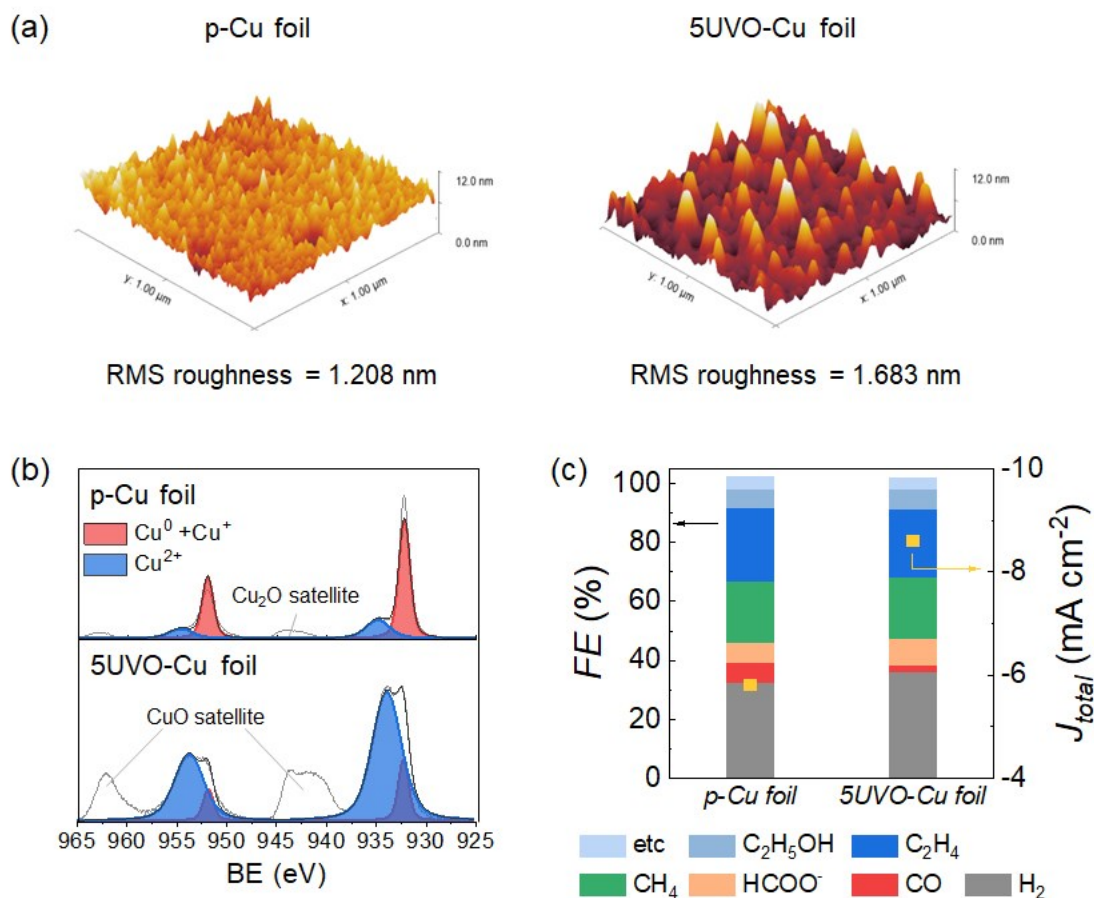


Figure S17. Characterizations of p-Cu foil and 5UVO-Cu foil. (a) AFM images of p-Cu foil (left) and 5UVO-Cu foil (right) having a root-mean-square (RMS) surface roughness of 1.21 nm and 1.68 nm, respectively. (b) XPS spectra of Cu 2p BE region showing Cu⁰&Cu⁺ (red) and Cu²⁺ signals (blue).⁶ (c) Current density (J_{total}) and selectivity of CO₂RR at -0.98 V vs. RHE. J_{total} of 5UVO-Cu foil is 1.5-fold higher than that of p-Cu foil. However, FE_{C₂+} for both electrodes is similar to 36%. Faradaic efficiency results show marginal disparity regardless of UVO treatment. The difference selectivity is only observed from C₁ products (CO and HCOO⁻) possibly influenced by surface hydrophilicity.¹⁵

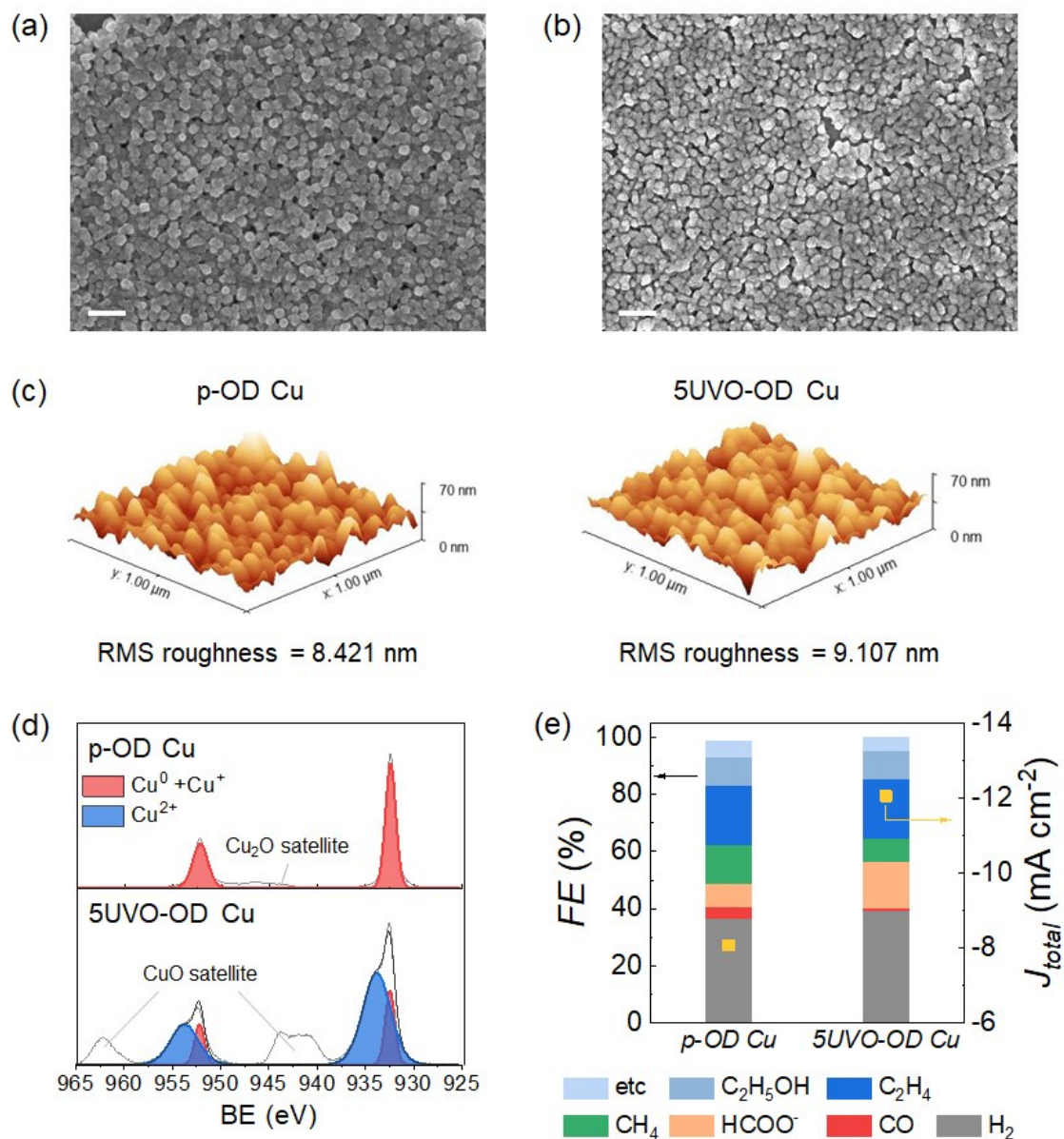


Figure S18. Characterizations of p-OD Cu NPs and 5UVO-OD Cu NPs. (a-b) SEM images of (a) p-OD Cu NPs and (b) 5UVO-OD Cu NPs. All scale bars indicate 200 nm. (c) AFM images of p-OD Cu NPs (left) and 5UVO-OD Cu NPs (right), providing an RMS surface roughness of 8.42 nm and 9.11 nm, respectively. (d) XPS spectra of Cu 2p BE region showing Cu⁰&Cu⁺ (red) and Cu²⁺ signals (blue).⁶ (e) Current density (J_{total}) and selectivity of CO₂RR at -0.98 V vs. RHE. J_{total} of 5UVO-OD Cu NPs is 1.5-fold higher than that of p-OD Cu NPs. However, FE_{C₂+} for both electrodes is similar to 35%.

	Cu ⁰ &Cu ⁺	Cu ²⁺
p-Cu foil	72.56%	27.44%
5UVO-Cu foil	14.39%	85.61%
p-OD Cu NPs	100.00%	0.00%
5UVO-OD Cu NPs	21.62%	78.38%

Table S5. Summary of atomic % of Cu⁰&Cu⁺ and Cu²⁺ from **Figure S17b** and **Figure S18d**. The p-Cu foil contained ~27.4% Cu²⁺ that was increased to ~85.6% after 5 h UVO treatment. The p-OD Cu NPs contained no Cu²⁺, and it was increased to 78.4% after 5 h UVO treatment.

FE (%)	p-Cu foil	5UVO-Cu foil	p-OD Cu NPs	5UVO-OD Cu NPs
CO	7.08	2.10	3.98	1.07
HCOO ⁻	6.81	8.94	8.12	16.37
CH ₄	20.59	20.88	13.68	8.30
CH ₃ OH	N.D.	N.D.	0.48	0.11
C ₂ H ₄	24.78	23.44	20.81	20.83
C ₂ H ₅ OH	6.64	6.67	10.13	9.73
acetate	0.91	0.67	0.53	0.31
acetone	0.56	0.28	0.48	0.24
ethylene glycol	N.D.	N.D.	0.03	0.10
allyl alcohol	N.D.	N.D.	N.D.	N.D.
glycolaldehyde	N.D.	N.D.	0.44	0.39
n-propanol	3.03	2.86	3.51	4.12
H ₂	32.31	36.06	36.41	38.98
Total	102.71	101.90	98.60	100.55

Table S6. Summary of Faradaic Efficiencies of Cu samples after 2 h CO₂RR at -0.98 V vs. RHE (**Figure S17c** and **S18e**). N.D. indicates 'not detected'.

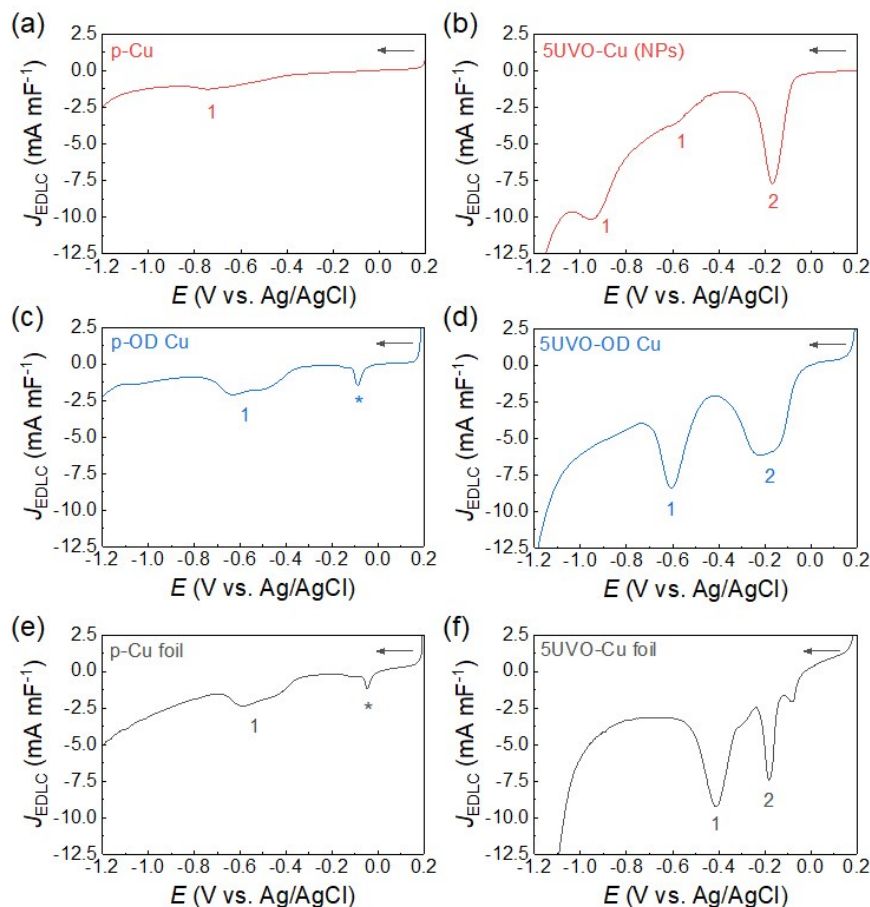


Figure S19. Cathodic linear sweep voltammograms (LSVs) of (a–b) Cu NPs, (c–d) OD Cu NPs, and (e–f) Cu foil electrodes. The left panel is pristine samples, and the right panel is 5UVO-treated samples. The electrolyte solution was Ar-purged 0.1 M KHCO_3 , and a scan rate was 10 mV s^{-1} . The arrow indicates the scan direction.

The Cu^+ (Cu_2O) reduction wave appears at $-0.4 \sim -0.7 \text{ V vs. Ag/AgCl}$ (**1**, $\text{Cu}^+ \rightarrow \text{Cu}^0$) in the pristine samples. The asterisk symbol indicates the deposition of Cu ion that was dissolved into the electrolyte solution at OCP.¹⁶ The 5UVO-treated samples exhibit the Cu^{2+} (CuO) reduction wave at $-0.15 \sim -0.23 \text{ V}$ (**2**, $\text{Cu}^{2+} \rightarrow \text{Cu}^+$) prior to the Cu^+ reduction. The predominant Cu^{2+} and Cu^+ for the 5UVO and pristine samples correspond to their high atomic % in XPS analysis, respectively (**Table 1** and **Table S5**). The Cu^+ reduction wave negatively shifts from the 5UVO-Cu foil to the 5UVO-Cu NPs (by -0.94 V), suggesting the sensitive Cu^+ reduction to the prior Cu^{2+} reduction, Cu structure, surface area, and capping ligand. The significant current increase below -1.0 V is attributed to the hydrogen evolution reaction.

	EDLC normalized (C mF ⁻¹)	A _{geo} normalized (C cm ⁻²)
Cu NPs	1.663	0.836
OD-Cu NPs	1.304	0.312
Cu foil	1.191	0.157

Table S7. Charge integration emerging during the cathodic reaction of copper oxides in the LSV curves (**Figure S19**), normalized to EDLC and geometrical surface area (A_{geo}). Comparable EDLC-normalized charge reflects a similar thickness of surface oxide layer, in contrast to the notable difference from the A_{geo}-normalized charge integration.

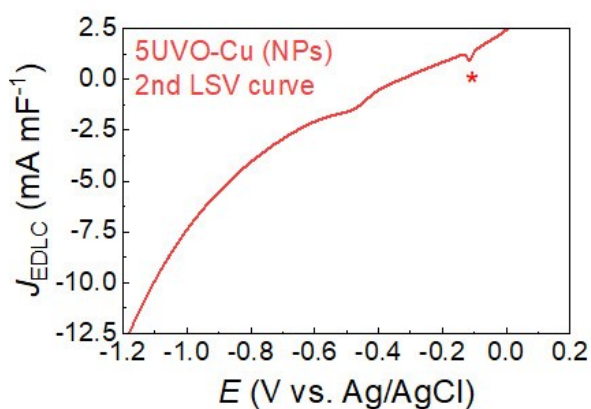


Figure S20. The second cycled LSV of the 5UVO-Cu, measured just after the first LSV without air exposure. The Cu²⁺ (CuO) cathodic wave disappears on the second cycle. In addition, the signal designated to the Cu ion redeposition (the asterisk symbol) emerges.

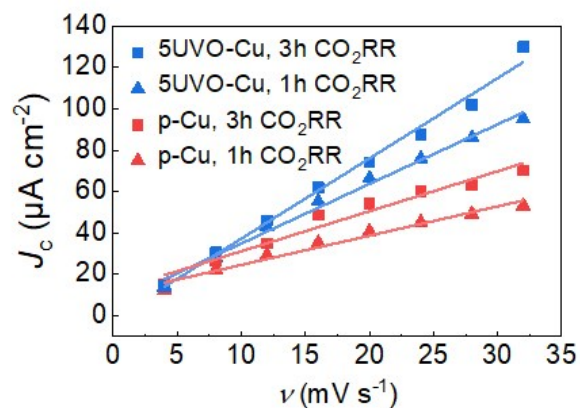


Figure S21. J_c plots as a function of scan rates (ν) at a potential of 0.18 V vs. Ag/AgCl for 5UVO-Cu (blue) and p-Cu (red) after 1 h and 3 h CO₂RR.

Catalyst _s	Condition	Capacitance ($\mu\text{F cm}^{-2}$)	R^2
p-Cu	before CO ₂ RR	2.57	0.997
	1 h CO ₂ RR	1415.65	0.970
	3 h CO ₂ RR	1931.26	0.965
5UVO-Cu	before CO ₂ RR	12.98	0.996
	1 h CO ₂ RR	2877.17	0.990
	3 h CO ₂ RR	3874.04	0.990

Table S8. Summary of calculated EDLC from J_c - ν plot in **Figure S21**. 5UVO-Cu shows higher capacitance than p-Cu, and both electrodes exhibited increasing EDLC for CO₂RR.

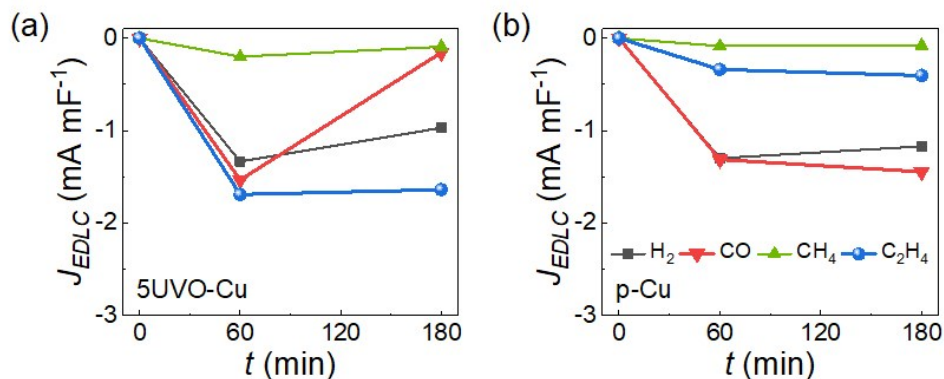


Figure S22. Partial current density (J), normalized by EDLC, towards gas products during 3 h CO_2RR on (a) 5UVO-Cu and (b) p-Cu at -0.98 V vs. RHE.

	Cu concentration (ppb)
As-prepared electrolyte solution (CO_2 -saturated 0.1 M $\text{KHCO}_3(\text{aq})$)	1.24 ± 0.88
Electrolyte solution after 3 h CO_2RR of p-Cu	16.12 ± 1.61

Table S9. ICP-OES analysis of Cu concentration from as-prepared 0.1 M $\text{KHCO}_3(\text{aq})$ electrolyte solution (CO_2 gas bubbled) and after 3 h CO_2RR of p-Cu. The Cu concentrations were measured three times. The dissolved Cu amount is less than 1%, considering the mass loading (~ 50 μg) of Cu NPs and the electrolyte volume (23 mL for the working electrode chamber).

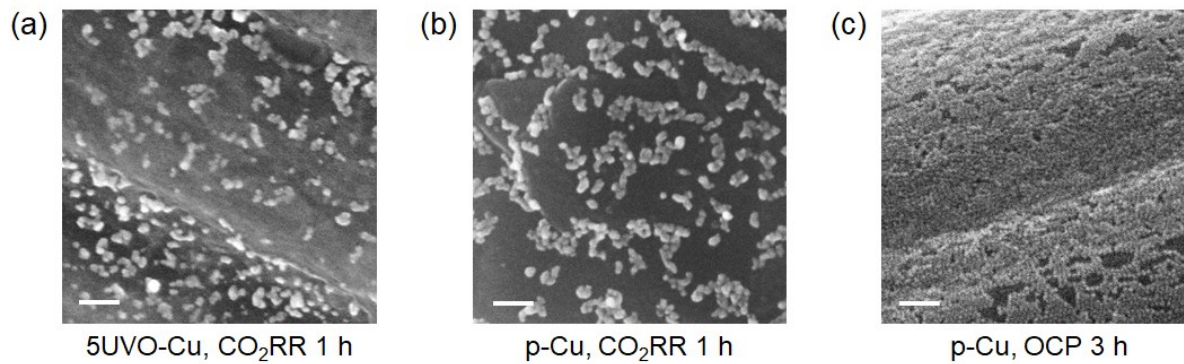


Figure S23. SEM images of (a) 5UVO-Cu after 1 h CO₂RR, (b) p-Cu after 1 h CO₂RR at -0.98 V vs. RHE, and (c) p-Cu immersing in CO₂-saturated 0.1 M KHCO₃ electrolyte solution at open circuit potential for 3 h. All scale bars indicate 100 nm.

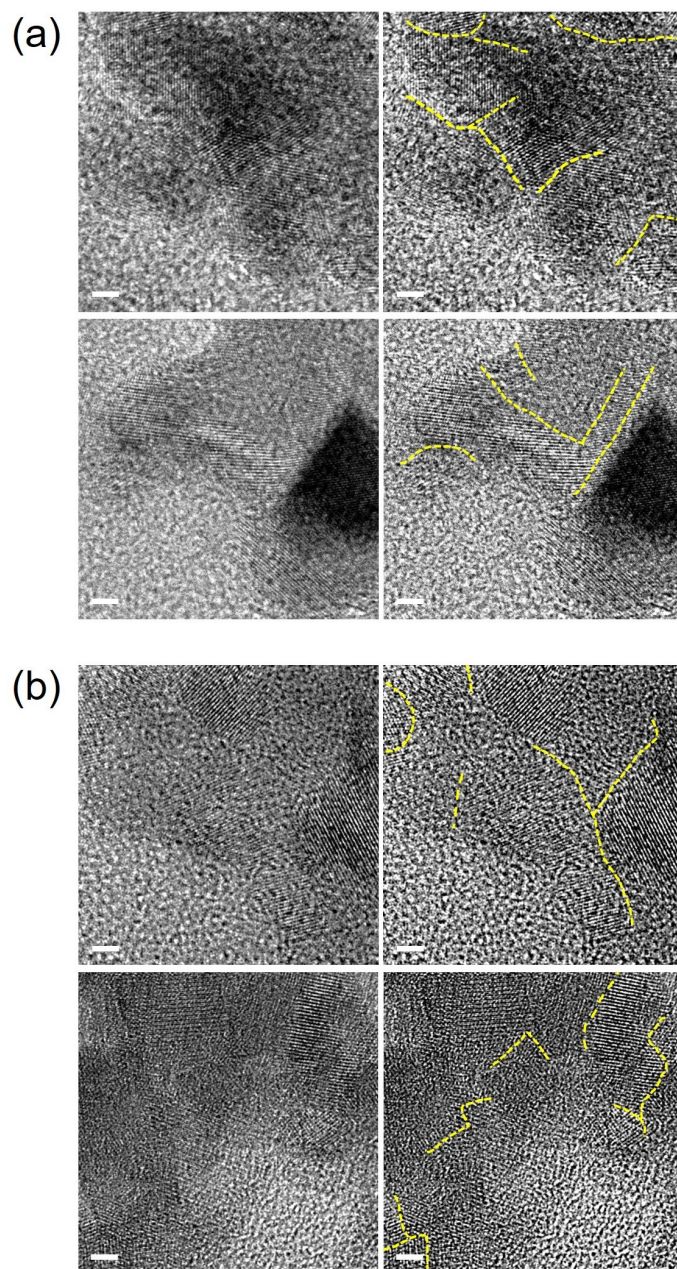


Figure S24. High-resolution TEM images for (a) 5UVO-Cu and (b) p-Cu with different positions after 3 h CO₂RR at -0.98 V vs. RHE. There are many grain boundaries at the interjunctions of Cu particles for both samples. The right panels of images include the artificial guidelines of grain boundaries. All scale bars indicate 2 nm.

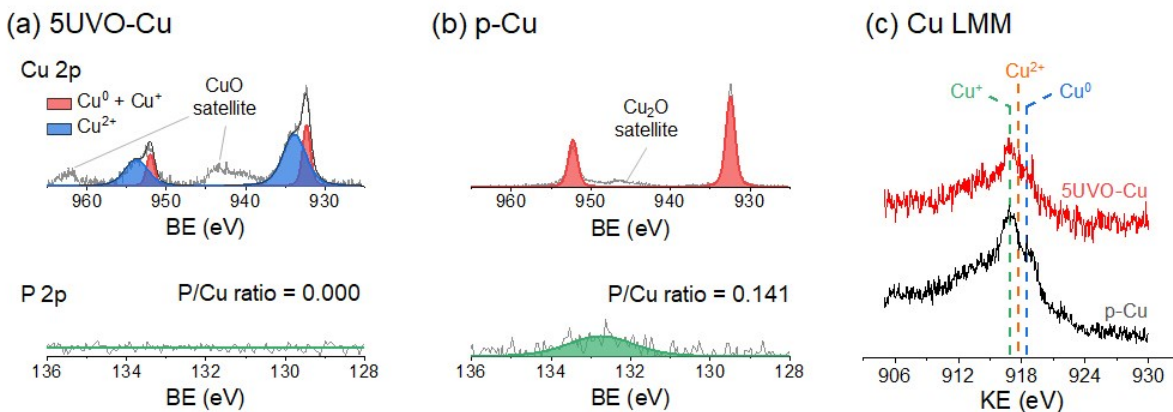


Figure S25. XPS spectra of Cu 2p and P 2p BE region of (a) 5UVO-Cu and (b) p-Cu after CO_2RR . The p-Cu has a residual capping agent ($\sim 50\%$) after the 20 h reaction. (c) Cu LMM Auger electron spectrum of 5UVO-Cu and p-Cu. The Cu catalysts were oxidized during sample drying for *ex situ* analysis. 5UVO-Cu contains all three phases of Cu, Cu_2O , and CuO, whereas the predominant Cu_2O and residual Cu are present in p-Cu.⁶

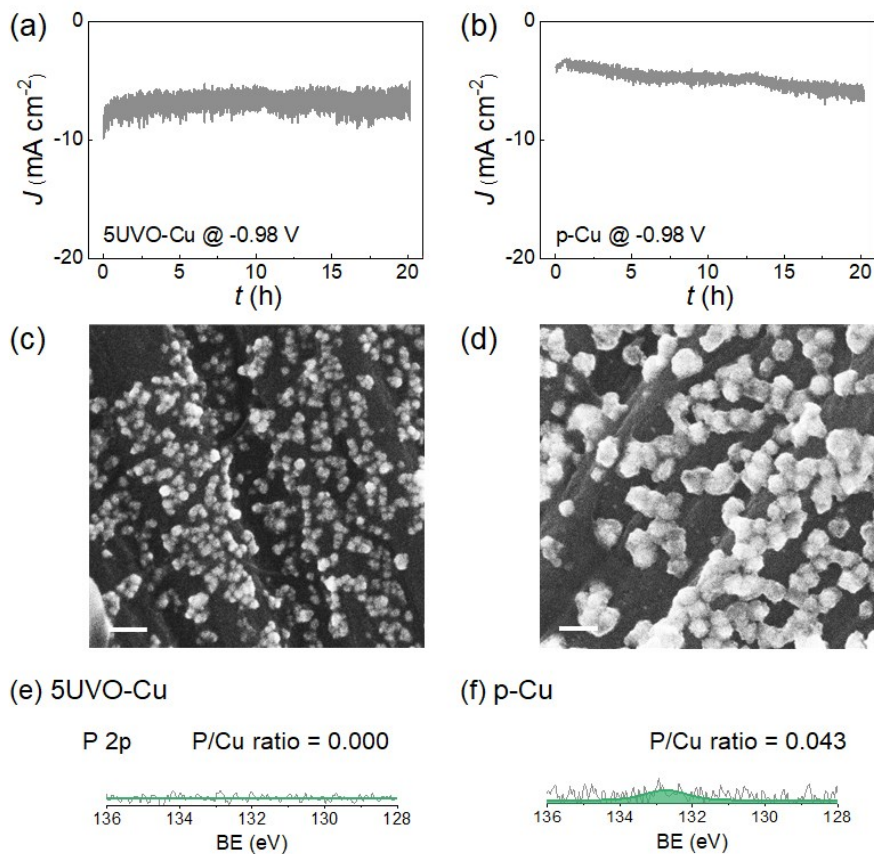


Figure S26. 20 h electrolysis under Ar-purged 0.1 M $\text{KHCO}_3(\text{aq})$ at -0.98 V vs. RHE. (a-b) Chronoamperogram under Ar-purged electrolyte -0.98 V vs. RHE for (a) 5UVO-Cu and (b) p-Cu. (c-d) SEM images of (c) 5UVO-Cu and (d) p-Cu after 20 h electrolysis at -0.98 V. 5UVO-Cu showed less agglomeration after 20 h catalysis, while p-Cu formed a sub-micron-sized polyhedron structure. All scale bars indicate 100 nm. (e-f) XPS spectra of P 2p BE region of (e) 5UVO-Cu and (f) p-Cu after 20 h electrolysis at -0.98 V vs. RHE. The p-Cu has a remnant capping agent ($\sim 17\%$) after the 20 h reaction.

Catalyst	Capping Ligand or surface treatment	Applied potential	Performance	Condition	Ref.
Cu NPs	tetradecylphosphonate	-0.98 V vs. RHE	FE _{C₂₊} =23%	0.1 M KHCO ₃ H-cell	This work
	ligand-free (UV-ozone)		FE _{C₂₊} =50%		
Cu NWs	oleylamine	-1.1 V vs. RHE	FE _{C₂H₄} =5.1%	0.5 M KHCO ₃ H-cell	17
	ligand-free (Photonic curing)		FE _{C₂H₄} =42.4%		
Cu-Ag core-shell NPs	oleylamine	-1.29 V vs. RHE	FE _{CO} =64.0%	0.5 M KHCO ₃ (cathodic side) 2 M KOH (anodic side), gas diffusion cell	18
	monoisopropylamine	-1.39 V vs. RHE	FE _{CO} =74.3%		
	surfactant-free (chemical treatment)	-1.25 V vs. RHE	FE _{CO} =73.0%		
(111)-dominant Cu ₂ O NPs	blank	-1.7 V vs. SCE	FE _{HCOO⁻} =40%	0.2 M NaHCO ₃ H-cell	19
	Br ⁻	-1.9 V vs. SCE	FE _{HCOO⁻} =60%		
	cetyltrimethylammonium bromide	-2.0 V vs. SCE	FE _{HCOO⁻} =90%		
Au NPs	ligand-free (thermal annealing)	-0.57 V vs. RHE	FE _{CO} =53%	0.1 M KHCO ₃ two-chamber cell	20
	<i>N</i> -heterocyclic carbene		FE _{CO} =83%		
Ag NPs	oleic acid	-0.75 V vs. RHE	FE _{CO} =87.8%	0.5 M KHCO ₃ two-chamber cell	21
	oleylamine		FE _{CO} =92.6%		
	dodecanethiol		FE _{CO} =65.2%		

Table S10. Summary of capping-ligand effects for selectivity of electrochemical CO₂ reduction.

References

1. D. Kim, C. S. Kley, Y. Li and P. Yang, *Proc. Natl. Acad. Sci.*, 2017, **114**, 10560.
2. L.-I. Hung, C.-K. Tsung, W. Huang and P. Yang, *Adv. Mater.*, 2010, **22**, 1910-1914.
3. D. B. Pedersen, S. Wang and S. H. Liang, *J. Phys. Chem. C*, 2008, **112**, 8819-8826.
4. G. H. Chan, J. Zhao, E. M. Hicks, G. C. Schatz and R. P. Van Duyne, *Nano Lett.*, 2007, **7**, 1947-1952.
5. T. Mokari, M. Zhang and P. Yang, *J. Am. Chem. Soc.*, 2007, **129**, 9864-9865.
6. S. Poulston, P. M. Parlett, P. Stone and M. Bowker, *Surf. Interface Anal.*, 1996, **24**, 811-820.
7. S. Pletincx, K. Marcoen, L. Trotochaud, L.-L. Fockaert, J. M. C. Mol, A. R. Head, O. Karslioglu, H. Bluhm, H. Terryn and T. Hauffman, *Sci. Rep.*, 2017, **7**, 13341.
8. Y. Ding, F. Zhang, J. Xu, Y. Miao, Y. Yang, X. Liu and B. Xu, *RSC Adv.*, 2017, **7**, 28754-28762.
9. A. M. Ferraria, J. D. Lopes da Silva and A. M. Botelho do Rego, *Polymer*, 2003, **44**, 7241-7249.
10. Y. J. Oh, J. J. Yoo, Y. I. Kim, J. K. Yoon, H. N. Yoon, J.-H. Kim and S. B. Park, *Electrochim Acta*, 2014, **116**, 118-128.
11. R. Lushtinetz, G. Seifert, E. Jaehne and H.-J. P. Adler, *Macromol. Symp.*, 2007, **254**, 248-253.
12. H. Li, B. Wu, C. Mu and W. Lin, *Carbohydr. Polym.*, 2011, **84**, 881-886.
13. H. Bo, T. Tarja and K. Eija, *Holzforchung*, 1997, **51**, 405-410.
14. P. Kappen, J.-D. Grunwaldt, B. S. Hammershøi, L. Tröger and B. S. Clausen, *J. Catal.*, 2001, **198**, 56-65.
15. A. K. Buckley, M. Lee, T. Cheng, R. V. Kazantsev, D. M. Larson, W. A. Goddard III, F. D. Toste and F. M. Toma, *J. Am. Chem. Soc.*, 2019, **141**, 7355-7364.
16. W. Tang, A. A. Peterson, A. S. Varela, Z. P. Jovanov, L. Bech, W. J. Durand, S. Dahl, J. K. Nørskov and I. Chorkendorff, *Phys. Chem. Chem. Phys.*, 2012, **14**, 76-81.
17. Y. Hou, S. Bolat, A. Bornet, Y. E. Romanyuk, H. Guo, P. Moreno-García, I. Zelocualtecatl Montiel, Z. Lai, U. Müller, V. Grozovski and P. Broekmann, *ACS Catal.*, 2019, **9**, 9518-9529.
18. E. Irtem, D. Arenas Esteban, M. Duarte, D. Choukroun, S. Lee, M. Ibáñez, S. Bals and T. Breugelmans, *ACS Catal.*, 2020, **10**, 13468-13478.

19. Y. Qiu, W. Xu, P. Yao, Q. Zheng, H. Zhang and X. Li, *ChemSusChem*, 2021, doi:10.1002/cssc.202100275.
20. Z. Cao, D. Kim, D. Hong, Y. Yu, J. Xu, S. Lin, X. Wen, E. M. Nichols, K. Jeong, J. A. Reimer, P. Yang and C. J. Chang, *J. Am. Chem. Soc.*, 2016, **138**, 8120-8125.
21. C. Kim, T. Eom, M. S. Jee, H. Jung, H. Kim, B. K. Min and Y. J. Hwang, *ACS Catal.*, 2017, **7**, 779-785.